Journal of Materials Chemistry A

ROYAL SOCIETY OF CHEMISTRY

PAPER

View Article Online
View Journal

Check for updates

Cite this: DOI: 10.1039/d5ta05646b

Bioderived and all-solution-processed tribolayer component enables adaptive design of flexible nanocellulosic triboelectric nanogenerators

Bushara Fatma, *[ad] Ioannis Ziogas,[b] Rishow Kumar,[c] Rami A. Elkaffas,[d] Ashish Garg,[e] Yarjan A. Samad,[dg] Leontios Hadjileontiadis,[bh] Blaise L. Tardy [f] and Charalampos Pitsalidis *[ag]

Triboelectric nanogenerators (TENGs) are emerging as key enablers for self-powered and wearable electronics, yet most state-of-the-art designs still rely on thick synthetic polymers and metal foils, which add bulk, limit flexibility, and complicate end-of-life disposal. Here, we report an all-solution-processed, polysaccharide-based TENG that combines an ultrathin nanocellulose (NC) tribolayer with a graphene electrode integrated on a flexible agar substrate. The entire active stack, fabricated *in situ via* continuous spray coating, measures approximately 10 micrometer in thickness, yielding a lightweight, mechanically stable, and conformable TENG platform. Various chemically and mechanically tailored cellulose nanomaterials are employed and systematically screened to maximize triboelectric output. Among the NC variants explored, never-dried cellulose nanocrystals (NDCNC) delivered the strongest performance, generating an open-circuit voltage of approximately 1070 V and a peak power density of 5.76 Wm^{-2}, values that outperform most natural-material-based TENGs reported to date. Moreover, relative to conventional TENGs with NC tribolayers that employ metal adhesive electrodes on synthetic substrates, our design achieved a three-fold boost in voltage output. The proposed NC-graphene-agar architecture is degradable as well as adaptable to a range of device layouts without requiring re-engineering of the underlying materials stack. The tribolayer is configured as a double-electrode TENG for high-output harvesting, and a single-electrode or zero-gap TENG for compact form factors. When integrated with the human body, the TENGs are able to harvest biomechanical motion and conduct real-time touch sensing. This adaptive design strategy enables application-specific customization while preserving the high-performance capabilities of the proposed TENG.

Received 13th July 2025
Accepted 6th November 2025

DOI: 10.1039/d5ta05646b

rsc.li/materials-a

Open Access Article. Published on 16 December 2025. Downloaded on 1/14/2026 9:01:06 PM. This article is licensed under a Creative Commons Attribution 3.0 Unported Licence.

1 Introduction

In recent years, wearable and implantable devices have marked a transformative shift toward ultrathin, soft, and conformable electronic components such as sensors, actuators, and energy-storing/-harvesting devices. Among these technologies, Triboelectric Nanogenerators (TENGs) have gained significant attention due to their ability to harness low-frequency mechanical energy distributed through environmental sources (*i.e.*, wind, waves, raindrops),[1–3] everyday human motion (*i.e.*, walking, jumping, tapping),[4,5] or even human physiological activity (*i.e.*, heartbeats).[6] This enables wearable devices and sensors to self-sustain, eliminating the need for bulky and uncomfortable power sources that require regular charging or battery replacement.[7] In addition, the inherent small form factor of TENGs can contribute to the development of wearable electronic devices designed for enhanced adaptability on human skin.[8,9] By integrating various sensing and energy-harvesting components into a shape-adaptive substrate, they can autonomously sense and respond to various external stimuli.[10–13] Besides performance and functionality, to fulfill the criteria for wearable technology, TENGs must have a quick response to mechanical deformation, sufficient breathability, and durability.[14,15]

Bioderived TENGs demonstrate remarkable versatility, striking a balance between processability, adaptability, and performance. As they are harvested from renewable sources

[a]Department of Physics, Khalifa University, Abu Dhabi, 127788, United Arab Emirates. E-mail: charalampos.pitsalidis@ku.ac.ae; bushara.fatma@ku.ac.ae
[b]Department of Biomedical Engineering, Khalifa University, Abu Dhabi, 127788, United Arab Emirates
[c]Department of Materials Science and Engineering, Indian Institute of Technology Kanpur, 208016, UP, India
[d]Department of Aerospace Engineering, Khalifa University, Abu Dhabi, 127788, United Arab Emirates
[e]Department of Sustainable Energy Engineering, Indian Institute of Technology Kanpur, 208016, UP, India
[f]Department of Chemical & Petroleum Engineering, Khalifa University, Abu Dhabi, 127788, United Arab Emirates
[g]Advanced Research and Innovation Center (ARIC), Khalifa University of Science and Technology, Abu Dhabi, United Arab Emirates
[h]Department of Electrical and Computer Engineering, Aristotle University of Thessaloniki, GR 54124 Thessaloniki, Greece

Open Access Article. Published on 16 December 2025. Downloaded on 1/14/2026 9:01:06 PM. This article is licensed under a Creative Commons Attribution 3.0 Unported Licence.

such as plants and shells (*i.e.*, chitosan and cellulose), they offer a greener alternative to synthetic polymers, reducing the environmental footprint associated with their production and offering a hazard-free end-of-life.[16] They are typically biodegradable and biocompatible, making them ideal for applications in wearable electronics and medical devices where environmental impact and human safety are critical considerations. Finally, the natural abundance and inherent soft properties of bioderived materials further enhance their appeal.[17] Through surface engineering and the use of solution-processing techniques, these TENGs can exhibit mechanical flexibility and responsiveness, thereby enhancing their ability to sense and convert biomechanical signals into electrical energy.[4] Also, this technology aligns with the principles of green electronics, utilizing eco-friendly, recyclable, and degradable materials to minimize environmental impact while promoting sustainability.[18]

Despite significant progress, most of the reported developments do not meet all the above-mentioned criteria. For example, several works emphasize environmentally friendly and degradable triboelectric layers but often rely on evaporated (or sputtered) metal electrodes and thick metal-coated adhesives.[19,20] In addition, a major concern arises from the substrate choice, as many state-of-the-art TENGs still rely on synthetic, non-biodegradable materials that pose both processing and environmental challenges. For example, polydimethylsiloxane (PDMS), polyvinylidene fluoride (PVDF), and polyethylene terephthalate (PET) have been widely used as triboelectric layers as well as substrates, although they suffer from cracking or adhesion issues, while flexible polyurethane is admittedly sensitive to environmental factors such as humidity and temperature.[21–24] Other promising flexible materials, such as silicone rubber or polyester, may cause skin irritation and limited breathability and pose environmental concerns.[18]

Among various bio-derived materials used as tribolayers, cellulose is undoubtedly the most widely used and the best-performing material, with a power density as high as 300 W m^{-2}.[25] Derived from various sources, cellulose is abundant and eco-friendly and can be chemically extracted into nanocellulose forms such as cellulose nanocrystals (CNCs) or cellulose nanofibrils (CNFs), resulting in high surface area and good mechanical properties. Cellulose-based materials can be processed through cost-effective methods and functionalized to enhance their triboelectric properties further. While cellulose materials typically exhibit high triboelectric performance, they are inherently positive, limiting pairing with other biopolymer-based tribolayers. Additionally, facilitating sufficient bonding between cellulose and electrodes or other support layers is challenging and can result in delamination. Finally, the processing and integration of cellulose in TENG formats often follow an assembly-type processing rather than an *in situ* layer-by-layer fabrication, resulting in rather bulky and thick TENG configurations.

We herein report on a systematic approach for developing ultrathin, all-solution-processed, bioderived tribocomponents designed for wearable electronic applications. These devices are constructed using polysaccharide-based substrate and tribolayer made of agar and NC, respectively, along with graphene electrodes, highlighting a sustainable alternative to conventional TENG designs. The fabrication follows an all-solution-processing route involving *in situ* spray-coating of the active layers. Through controlled deposition, an ultrathin (~6 μm) NC tribolayer and a graphene electrode (~4 μm) integrated into the flexible agar substrate is achieved. This direct integration eliminates the need for conducting adhesives, improving interfacial uniformity and ensuring optimal performance. The resulting devices demonstrate excellent output capabilities, with a peak voltage of ~1070 V and a peak power density of ~5.76 W m^{-2}. In addition, the proposed triboelectric component is successfully integrated into an all-bioderived TENG, demonstrating one of the highest performances ever reported for such systems. Finally, their touch-sensing capabilities were validated through press-and-release tests, where finger-worn TENGs were effectively used to distinguish signals from various materials.

2 Materials and methods

2.1 Materials

Polyimide (PI) films were purchased from Agar Scientific and agar from Sigma-Aldrich. Milli-Q (MQ) water was collected from a Millipore Milli-Q purification system. Ethanol (94%) and isopropyl alcohol (IPA) were obtained from Sigma-Aldrich. PET films (Mylar) were purchased from the local market of UAE. All the reactants and solvents were used as received without any further purification treatment.

2.2 Preparation of various types of nanocellulose

The NCs reported in this work were produced from different sources and extraction processes, including mechanical and chemical treatments. All NC-based samples were used as concentrated dispersions except for the spray-dried one used in powder form. The preparation details of never-dried cellulose nanocrystal (NDCNC), cellulose nanofibril (CNF), spray-dried cellulose nanocrystal (SDCNC), and tempo-oxidized cellulose nanofibril (TOCNF) are mentioned in the supporting information (SI) file (Section S1).

2.3 Preparation of graphene ink

Fabrication details are mentioned in the SI (Section S2).

2.4 Substrate and film processing

2.4.1 Agar substrate preparation. For the fabrication of the agar substrate, agar powder was added to DI water to make 30 mL of a 2 wt% mixture along with 0.2 mL of glycerol. The solution was boiled thrice in a microwave oven operating at 600 W for 1 min. A viscous agar solution was then cooled to 60 °C before pouring it into a Petri dish. Then, the resulting material was kept at 60 °C overnight to allow the remaining water to evaporate sufficiently. Finally, a transparent, flexible, and free-standing agar film was extracted and stored at room temperature with a relative humidity of 50%.

2.4.2 Graphene deposition on agar substrates. For the preparation of the graphene-coated agar substrate, the untreated

 This journal is © The Royal Society of Chemistry 2025

Open Access Article. Published on 16 December 2025. Downloaded on 1/14/2026 9:01:06 PM. This article is licensed under a Creative Commons Attribution 3.0 Unported Licence.

agar was fixed onto the heating plate at 60 °C using Scotch tape. In each pass, the preheated substrate was sprayed with graphene ink as the nozzle of the spray gun moved from one end to the other, and the process continued until the entire surface was covered. A layer-by-layer coating of graphene ink was performed for 40 passes. The total thickness of the graphene coating was found to be ~4 μm (one pass corresponds to 100 nm) as measured by the cross-sectional FESEM of freeze-fractured samples.

2.4.3 NC deposition on graphene-coated agar substrate. For making an ultrathin triboelectric layer, NC dispersion with the desired concentration was sprayed onto a graphene-coated agar substrate without any surface treatment. The spraying process was followed as discussed in the above-mentioned section. The spraying process was repeated for 80 passes, and a layered NC film was prepared with a thickness corresponding to ~5–6 μm (each pass is equivalent to 63–75 nm). Therefore, the total thickness of the active component is onto the agar substrate is estimated to be ~10 μm.

2.4.4 Preparation of castor oil (CO)-based film. Details regarding the preparation of CO-based film has been recently reported by us and is mentioned in detail in the SI (Section S3).[26]

2.5 TENG device configurations

TENGs with NC films of different origins and different processing methodologies (different surface functional groups) were deposited onto the graphene-coated agar substrates. The complete TENG device is named NC–Gr–A TENG. For comparative purposes, the same NCs were also tested using conventional Cu adhesive on PET substrates (Section S4).

2.5.1 NC–Gr–A TENG. The NC–Gr–A tribolayer was made of agar, graphene, and NCs as substrate, electrode, and triboelectric layer, respectively. The NC at the top was placed opposite to the counter negative triboelectric layer. The negative triboelectric layer in the two-electrode device configuration was made of PI/Cu/PET.

2.5.2 NC–CO bio-TENG. For the preparation of bioderived TENG, NC–Gr–A was used as a positive triboelectric component, whereas a biopolymer-based film made of the modified CO film was used as a negative tribolayer. Information about the preparation of the CO film can be found in our recently published work.[26]

2.5.3 All-PS SE-TENG. All-polysaccharides single electrode (SE-TENG) TENG was based on a single NC–Gr–A tribocomponent operated against various electrode-free surfaces.

2.6 Characterization of films and device measurement

The XRD characterization of the different NC films and the triboelectric component was performed using X-ray diffraction (Panalytical MRD Pro X-ray Diffractometer). The cross-sectional thickness study of the triboelectric component was done using a JEOL SEM. The sample was freeze-fractured using liquid nitrogen and coated with a thin gold layer before imaging. A thermogravimetric analyzer (TGA Q50, USA) was used to obtain the thermal properties of the films by analyzing the thermal weight change. The samples were kept in a platinum crucible and heated in a furnace at a heating rate of 10°C min^{-1} in an N_2 environment (40 mL min^{-1}). The elemental composition analysis of the NC films was carried out using XPS (PHI 5000 Versa Prob II,FEI Inc). The mechanical properties (tensile stress and strain (%)) were obtained using a Universal Testing Machine. Rectangular samples for tensile testing were prepared according to ASTM Standard D882, with a gauge length and width of 3 cm (5 cm total length) and 1 cm, respectively, at a crosshead speed of 1 mm min^{-1}. A Four-Point Probe (Ossila P2010A2) setup was used to measure the sheet resistance and conductivity at different positions on the spray-coated graphene substrate. The average value was determined, and the measurement was repeated for three bending cycles: 0, 15 000, and 30 000. For the cyclic bending of spray-coated graphene, a rectangular sample with dimensions of 4 cm in length and 1 cm in width was fixed onto a larger PET sheet, which was then bent and released continuously using an automated setup. The static and dynamic contact angles were measured by placing a 10 μL deionized water droplet on agar and PET substrate using a dispensing syringe. When the droplet stabilized, images of the water droplet were captured using a Contact Angle Goniometer (Ossila, UK) and contact angle measurements were performed using the Ossila Contact Angle application. The open-circuit voltage of the TENG during external force-driven contact and separation of the positive and negative triboelectric layers was measured using an oscilloscope (Tektronix TBS 1072B). A compressive pressure of 0.4 MPa was applied using a custom-built automated linear motion-based testing setup for TENG characterization. The biomechanical energy harvesting and material sensing experiments were tested by only one participant, the first author (B.F) of this paper. Informed consent was obtained for the experiments involving human participant (s). The experiments were performed in compliance with the relevant institutional (KU) guidelines and regulations. The study protocol was reviewed and approved by the Institutional Review Board/Ethics Committee. Ethical approval reference/permit number: 2507000549. The water vapor transmission rate of the samples was obtained using the ASTM standard with an inverted cup model E 95–96. Initially, a glass bottle was filled with reverse osmosis water, and then films were mounted onto the rim of the filled glass bottle using double-sided tape. An uncovered, water-filled bottle and PVDF film were used as positive control and negative control, respectively. We have also used A4 printing paper and a lab coat textile for comparison. The weight of all the filled bottles with mounted films was obtained and followed by measuring the weight change of the same bottles after 24 h continuously for 7 days. The WVTR was calculated using the slope g/t of the weight change *vs.* time curve as mentioned below.

$$\mathrm{WVTR} = g/(t \times \text{area of film})$$

3 Results and discussion

3.1 NC–Gr–A tribocomponent with ultrathin-sprayed active layers

The step-by-step process for the fabrication of the all-solution-processed TENGs is shown in Fig. 1a. Specifically, the proposed triboelectric component was prepared *via* layer-by-

Open Access Article. Published on 16 December 2025. Downloaded on 1/14/2026 9:01:06 PM.
This article is licensed under a Creative Commons Attribution 3.0 Unported Licence.

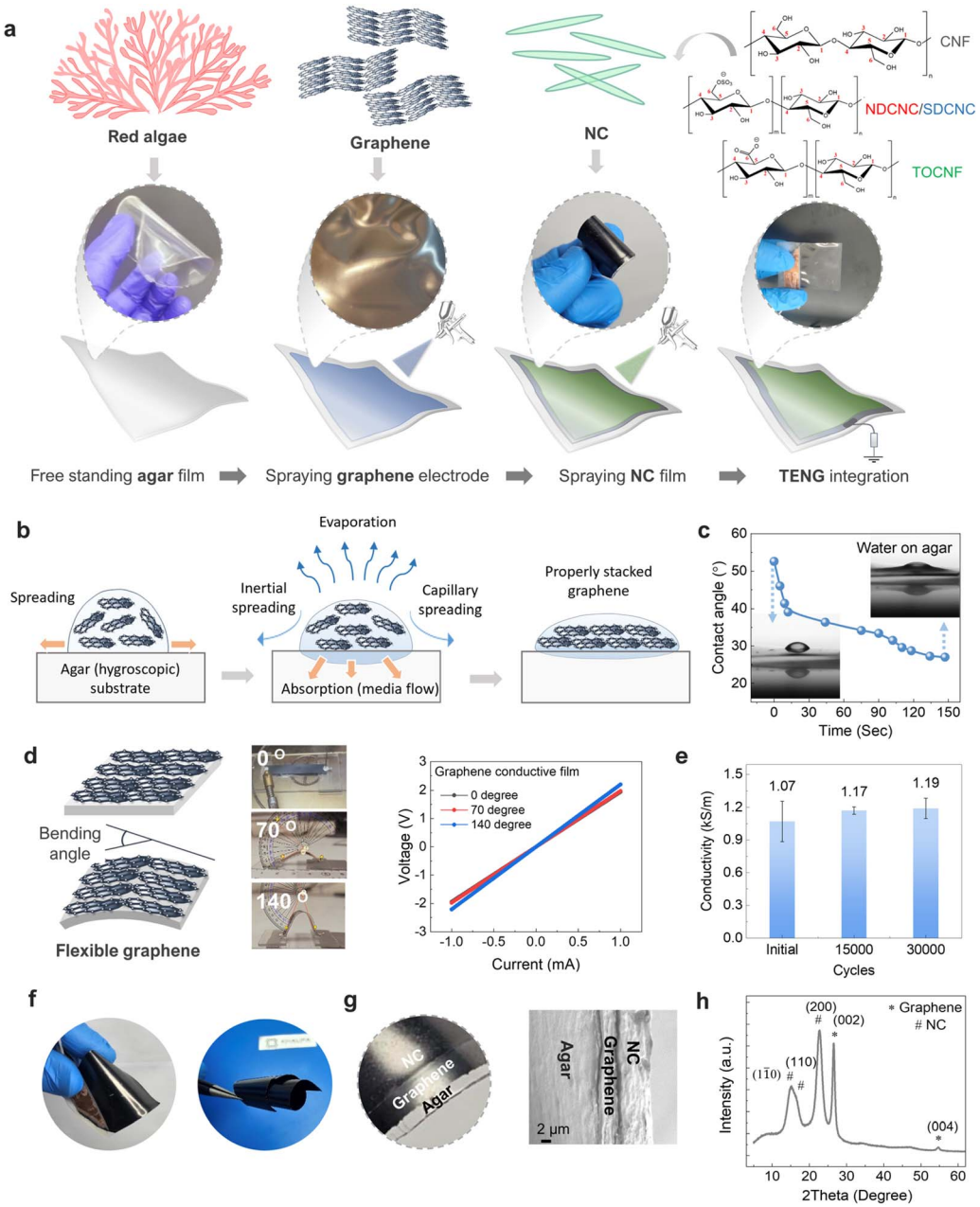

Fig. 1 (a) Schematic illustration of the step-by-step fabrication process for the NC–Gr–A triboelectric component, accompanied by photographic images of each stage. The sequence highlights the flexible and transparent agar film originating from red algae, the spray-coated graphene layer onto agar substrate, and the completed flexible NC–Gr–A triboelectric component after depositing the NC layer on the graphene-coated agar. The figure also shows the schematic of the chemical structure of various NCs (CNF, NDCNC, SDCNC, and TOCNF) (b) deposition mechanism of spray-coated ultrathin graphene on agar substrate. (c) Graph showing the change of water CA values over time for the graphene on agar, along with the corresponding photographic images at 0 and 147 seconds. (d) Schematic representation of the bending angles for the graphene-coated substrate and the effect of various bending angles on the *I*–*V* curve of the ultrathin graphene layer. (e) The histogram displays the conductivity values of the graphene electrode measured at various bending cycles (0, 15 000, and 30 000 cycles). (f) Photographic images of NC–Gr–A triboelectric component with ultrathin graphene electrode and NC-based active layers exhibiting foldability and rollability, demonstrating their flexible and conformable nature. (g) Top-view photograph and cross-sectional FESEM image of NC–Gr–A for visualization of the layer stacking. The NC sample used is NDCNC (h) X-ray diffractogram of the NC–Gr–A component. The NC shown in the characterization of the NC–Gr–A tribolayer is NDNC.

layer spray coating of graphene on a flexible agar substrate, followed by a multilayered coating of NC (NC–Gr–A). Specifically, NCs used here were based on CNF obtained by mechanical fibrillation, NDCNC and SDCNC and TOCNF. Fig. 1a shows the chemical structure of CNF, NDCNC, SDCNC, and TOCNF. The surface of CNF has hydroxyl (OH^-) groups, NDCNC and SDCNC are sulfated nanocrystals (OSO_3^-) with the surface having at the primary surface hydroxyls (sulfate ester group) along with OH^-

This journal is © The Royal Society of Chemistry 2025

Open Access Article. Published on 16 December 2025. Downloaded on 1/14/2026 9:01:06 PM. This article is licensed under a Creative Commons Attribution 3.0 Unported Licence.

groups, whereas TOCNF are carboxylated cellulose nanofibrils with COO^- at the primary surface hydroxyls and secondary hydroxyl groups. Agar, derived from marine algae, forms a gel-like consistency upon hydration, enabling it to conform seamlessly to various surfaces, including human skin, without causing adverse skin effects (*i.e.*, irritation).[27] To exploit these functionalities, agar substrates were prepared through solution casting and molding, resulting in transparent and flexible substrates (See Fig. 1a and S1). The mechanical stability of the agar substrates was assessed using tensile measurements. The material was found to retain sufficient tensile strength without compromising its flexibility, ensuring durability under various stress conditions. As shown in Fig. S2, the measured substrate yielded a tensile strength of 24.6 MPa with a strain at break of 4.9%, indicating that the mechanical performance of agar aligns well with previously reported data, further confirming its suitability for flexible electronics.[28] To prepare and integrate the electrode of the tribocomponent, graphene suspension was directly sprayed onto the agar substrate without further surface modification. The spraying process involved 40 passes, with continuous drying between each pass until a homogeneous coating was visibly formed on the surface.

For comparison, a commercially available PET sheet was also employed as a substrate and coated with graphene using the same method. Both substrates showed a complete coverage over a large surface area (90 mm), with the graphene-coated agar exhibiting a more metal-like appearance compared to graphene-coated PET. This difference can be attributed to the improved wettability of the agar surface, which facilitates better surface absorption and enhances the stacking and interconnection of graphene nanosheets (see Fig. 1b). This is further confirmed by the water contact angle (CA) measurements. Specifically, Fig. 1c reveals a dynamic CA response, with values decreasing from 52.6° to 27.0° over a duration of ~147 s, due to water spreading and absorption resulting from the hygroscopic nature of agar (see Fig. S3). Conversely, the PET substrate exhibits a less hydrophilic behavior, with water CA values of ~78.4°, as shown in Fig. S4. This may cause non-uniformities in the graphene coating during the spraying process due to the "coffee-ring" effect, where droplet edges are pinned onto the substrate upon rapid drying (Fig. S5). This may account for the graphene layer adopting a more metallic appearance on agar compared to PET.

The quality of the graphene coatings was further investigated using four-probe electrical measurements. Based on the IV curve shown in Fig. S6, the conductivity of graphene on agar appears to be significantly higher than that on PET. Specifically, the conductivity of graphene on agar is 1070 ± 184 S m^{-1}, whereas the conductivity of graphene on PET is 740 ± 96 S m^{-1}. Considering the criteria for device wearability, we also performed a bending test to ensure that the performance and durability of the conductive electrode are coupled with conformability. For that, the Gr–A substrates were subjected to different bending angles, with the angle between the tangents drawn onto the switch and the face of the substrate, as shown schematically in Fig. 1d. The IV curve at different bending angles overlaps, and therefore, the conductivity of graphene remains relatively stable across various bending angles, including 0, 70, and 140°. The voltage variation ($V_0/V \times 100$, where V_0 is the voltage in the absence of bending) is negligible at 70°, while only a minimal effect can be observed for extreme angles of 140° (Fig. S7). The stability of graphene on agar was evaluated by subjecting the films to repeated bending cycles of up to 180°. Electrical conductivity (Fig. 1e) and sheet resistance (Fig. S8) were monitored throughout the tests, revealing no significant change in conductivity even after 30 000 cycles. This level of stability suggests that, under prolonged mechanical bending stress, the graphene layer maintains its electrical performance.

AFM was used to examine the surface topography of graphene deposited on both agar and PET substrates. The scans revealed comparable surface roughness values, indicating that graphene exhibits a similar micromorphology on both substrates (Fig. S9). Nevertheless, it should be noted that the aerosol droplets deposited during the spraying process are typically much larger than 10 μm, meaning any macroscale thickness variations or coverage gaps may fall outside the AFM scan area.

Regarding thermal stability, the thermal response of the graphene-coated agar exhibited the same degradation pattern, with only a slight increase of approximately 5 °C compared to the pure agar substrate (Fig. S10).

Multilayered spraying of the NCs on top of the Gr–A substrates resulted in homogeneous and complete NC layers, even after several spraying passes, without visible defects or macroscopic deformations. On the contrary, sprayed layers appeared to delaminate after a few tens of passes when the same multilayered processing was used with PET substrates (Fig. S11). Moreover, as shown in Fig. 1f, the NC–Gr–A exhibits excellent foldability and rollability, which are crucial for wearable and/or conformable electronics. Fig. 1g shows the top and cross-sectional view of the active layers on the agar substrate. Layers of Gr and NC are visible in the photographic image of the top surface. As shown in the cross-sectional FESEM image of the stratified structure of the NC–Gr–A, the active layers, including the Gr electrode and NC layer, have thicknesses of approximately 4 μm and 6 μm, respectively, resulting in a total thickness of around 10 μm. Considering the number of spraying passes and the overall thickness, each sprayed layer corresponds to ~100 nm and 75 nm for Gr and NC, respectively. The film stacking and formation for all NC–Gr–A are shown in the FESEM images of Fig. S12. This confirms the versatility of the layer-by-layer technique for the *in situ* deposition of both the electrode and the tribolayer.

The structural characterization of the NC–A–Gr (with NDNC coating) was performed using XRD (see Fig. 1h). The XRD diffractogram of the overall tribocomponent revealed a series of characteristic peaks corresponding to NC and graphene. The diffraction peaks at 2θ equals to 15.1°, 15.7° and 22.5° corresponding to $(1\bar{1}0)$, (110) and (200) planes of NDCNC (cellulose I).[29] Peaks at 26.5° and 54.5° correspond to the (002) and (004) graphene planes, respectively, which agrees with previously reported XRD data for exfoliated graphene prepared using mechanical treatments, such as applying shear forces or sonication. The peak positions of exfoliated graphene are consistent

Open Access Article. Published on 16 December 2025. Downloaded on 1/14/2026 9:01:06 PM.
This article is licensed under a Creative Commons Attribution 3.0 Unported Licence.

with the graphitic planes, with an apparent peak broadening typically observed in exfoliated graphene.[30,31]

3.2 NC–Gr–A TENG

Going one step further, the NC–Gr–A tribolayers were used to fabricate TENG devices. Fig. 2a shows a schematic of the TENG device architecture with NC–Gr–A as the positive triboelectric component and PI as the negative tribolayer, along with the corresponding photographs. Given that the NC–Gr–A system has not been previously studied, its response in both forward and reverse modes was measured to ensure proper TENG operation. The voltage output of the CNF-based NC–Gr–A TENG was measured at 906 V (Fig. 2b) and remained consistent upon changing the electrode polarity, confirming the efficient TENG function. The TENG's output voltage of the various NC–Gr–A *versus* PI is shown in Fig. 2c. NDCNC-based NC–Gr–A TENG yielded the highest performance with a peak voltage output of approximately 1070 V, followed by the CNF (~906 V). SDCNC and TOCNF-based TENGs exhibited an overall decrease in the output voltage with values of approximately 760 V and 450 V, respectively. The performance alterations across the various NCs can be primarily attributed to the differences in their

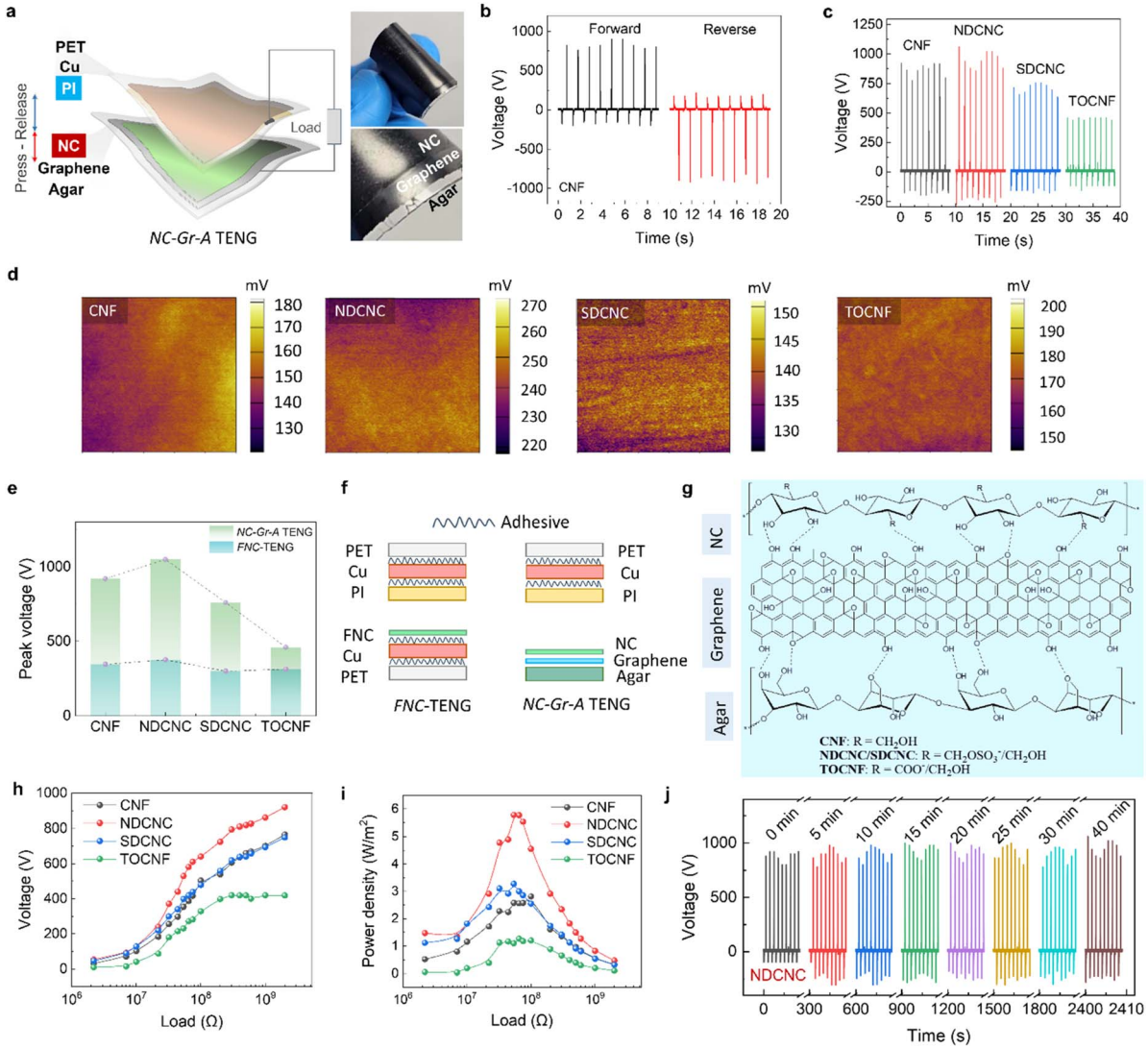

Fig. 2 (a) Schematic representation of the NC–Gr–A dual-electrode TENG, prepared using a positive triboelectric component with ultrathin active components (graphene and NCs) against PI as a negative tribolayer. Corresponding photographs showing the different layers of NC–Gr–A. (b) Voltage output response of CNF-based NC–Gr–A TENG, operated in forward and reverse mode. (c) Voltage output of NC–Gr–A TENG made of CNF, NDCNC, SDCNC and TOCNF. (d) KPFM of the corresponding NC films showing their surface static potential. (e) Bar graph showing the difference in voltage output of FNC-TENG and NC–Gr–A TENG for ultrathin NC films made of CNF, NDCNC, SDCNC, and TOCNF. (f) Schematic showing the difference in device structures with a focus on the use of adhesive and ultrathin structure. (g) Chemical structure of NC–Gr–A component depicting the physical interaction between the interfacial strength and stability of the layered structure. (h) Variation of voltage output and (i) the corresponding power density of the different NC–Gr–A TENGs with varying load resistance values ranging from 2 MΩ to 2 GΩ. (j) Time-dependent voltage output for the best-performing (NDCNC-based) NC–Gr–A TENG, continuously operated for 40 minutes and each data is recorded for 10 seconds every 5 minutes.

 This journal is © The Royal Society of Chemistry 2025

Open Access Article. Published on 16 December 2025. Downloaded on 1/14/2026 9:01:06 PM. This article is licensed under a Creative Commons Attribution 3.0 Unported Licence.

electron affinity, as highlighted by the variations in the surface potential observed through KPFM. Fig. 2d shows the corresponding surface potential maps (in a 5 μm × 5 μm area), revealing that the surface potential of all NC films is positive and reaches a few hundred mV, consistent with the reported literature.[32,33] The highest surface potential is obtained for NDCNC, which is approximately 100 mV more positive as compared to CNF and SDCNC. Moreover, TOCNF also exhibits a slight increase in surface potential compared to CNF and SDCNC. This confirms that all NC films can be used as a positive triboelectric layer. The preparation conditions can alter the functional groups on the cellulose surface and, therefore, can further tune the surface potential of the triboelectric layer. The high electrostatic surface potential of NDCNC is attributed to its sulfonic acid functional groups. These moieties introduce additional deep trap states, thereby increasing the charge-trapping sites and promoting more efficient accumulation and long-term retention of triboelectric charges within the nanocellulose dielectric layer.[34]

Introduction of polar molecules with symmetrical distribution of electrostatic potential results in an increase in the deep trap density of the polymer and, therefore, increases its charge trapping ability. The electrostatic potential of the sulfonic functional group in NDCNC is symmetrically distributed, thereby increasing the deep trap density and enhancing its ability to trap charges, which in turn increases the electrical output of NDCNC-based TENGs. Wang *et al.*[34] confirmed this by performing density functional theory (DFT) calculations, which show that if the electronic band gaps of grafted molecules overlap with those of the grafted polymer molecules, it can act as deep traps to increase the modified polymer's ability to trap charges. Indeed, DFT calculations of NC and sulphonated NC reveal that the electron orbitals of the sulfonic functional group are located within the electronic band gap of the NC macromolecule, allowing it to act as a deep hole trap. Therefore, they can capture and immobilize charge carriers, rather than allowing them to immediately recombine or dissipate. Therefore, the surface functionalization of nanocellulose may alter the electronic band structure and polarization landscape, enabling the formation of deeper and denser traps. This increases both the dielectric property and the effective electron affinity, which is quantitatively expressed as a higher surface potential, thus enhancing device performance.

SDCNC, on the other hand, has fewer sulfonic acid functional groups than NDCNC and therefore relatively lower deep trap density, resulting in lower TENG performance. According to the literature, pristine CNF bearing only hydroxyl groups may possess a lower density of deep-trap states. As a result, its surface potential and triboelectric performance are expected to be inferior to those of sulfonated SDCNC.[34] Surprisingly, CNF exhibits higher performance than SDCNC, most likely due to the presence of OSO_3^-, which could be introduced *via* sodium dodecyl sulfate during its preparation. Therefore, NDCNC and CNF both have an improved charge trapping ability for induced surface static charges compared to SDCNC. Regarding TOCNF TENG, although the surface potential is rather high, its performance is low. This can likely be associated with the low interfacial interaction with graphene. In addition, as shown in Fig. S13b, TOCNF appeared to be crumbled, most likely due to its highly crystalline content and mechanical rigidity.[35] This was further confirmed during the TENG device measurement, where the TOCNF layer tends to delaminate easily after only a few testing cycles (Results not shown here).

It can be observed that the voltage signal of the TENG exhibits significant asymmetry, which may be caused by the abrupt separation between the triboelectric layers triggered by adhesion.[36] Commonly known as the "sticking effect," this intrinsic adhesion phenomenon is mainly caused by electrostatic interactions between opposing triboelectric charges on the contacting surfaces. This sticky behaviour is further enhanced by intermolecular interactions, such as van der Waals forces and/or other surface-specific interactions. These collective adhesion forces significantly alter the input mechanical motion profile after initial contact, causing the triboelectric layers to abruptly and impulsively separate. The peak voltage amplitude in the corresponding half cycle of the voltage output signal is thus significantly increased by this quick detachment, which also improves the instantaneous charge transfer. Additionally, other contributing factors, such as the thickness of the dielectric layer, device operating conditions, and the distance between the triboelectric layers, may also impact the observed voltage asymmetry. Therefore, when transitioning from a separation to a contact state, the low voltage output in the other half cycle is primarily due to the thin layer of dielectric NC film.[37] Therefore, together with adhesion-driven impulsive behaviour, these experimental parameters determine the TENG's unique asymmetrical output properties.[37–39]

To further highlight the significance of our design strategy, free-standing nanocellulose (FNC)-based TENGs were fabricated using a conventional configuration employing Cu adhesive electrodes and a PET substrate. The fabrication details and output characteristics of the FNC-TENG are provided in Section S5 (see also Fig. S13). Notably, the proposed NC–Gr–A TENGs exhibited consistently higher voltage outputs compared to the FNC-TENG counterparts across all NC types (Fig. 2e), achieving approximately a threefold enhancement, from 375 V to 1070 V, in the case of the NDCNC. The reliance on adhesive electrodes in FNC-TENGs often introduces interfacial defects during layer stacking, particularly in the case of ultrathin films that are challenging to handle in a free-standing form (Fig. 2f). On the contrary, the superior performance of the NC–Gr–A TENG can be attributed to the direct layer-by-layer deposition of graphene and NC onto the agar substrate, which enables precise control over film thickness and uniformity while promoting strong interfacial adhesion and seamless integration among the dielectric, electrode, and substrate layers. This structural coherence enhances surface-to-surface interactions, reducing interfacial resistance and facilitating more efficient charge separation and transfer. In addition, substituting the Cu adhesive electrode with a layered graphene also enhanced conformability, leading to a ~15-fold reduction in overall thickness, from 66 μm for Cu to 4 μm for the graphene layer.

To assess the interfacial strength and mechanical stability of the NC–Gr–A component, a standard "scotch" tape test was

Open Access Article. Published on 16 December 2025. Downloaded on 1/14/2026 9:01:06 PM. This article is licensed under a Creative Commons Attribution 3.0 Unported Licence.

conducted (See Video S1). In this test, the adhesive part of a tape was repeatedly applied to and peeled from the top of the NC–Gr–A surface (see Fig. S14a). Interestingly, the NC–Gr–A triboelectric component remained intact after multiple cycles, without any cracks or signs of delamination, indicating good interfacial bonding between the constituent layers. Specifically, the layers are physically integrated with their interfacial adhesion governed by extensive hydrogen bonding among the abundant surface –OH groups present across agar, graphene, and NC layers (Fig. 2g). This network of hydroxyl-mediated interactions reinforces mechanical cohesion at the Gr–A and NC–Gr interfaces while preserving the ultrathin, flexible capabilities of the TENG.

FTIR spectroscopy was performed to confirm the type of intermolecular interaction contributing to the improved surface adhesion of the NC–Gr–A films. As shown in the FTIR spectrum of Fig. S14b, NC exhibits a peak at ~3333 cm^{-1}, characteristic of the O–H stretching vibration. In the case of NC–Gr–Agar layer, the broad O–H stretching band becomes slightly red-shifted, indicating hydrogen bonding interactions between hydroxyl groups of NC and agar chains, as well as with oxygen-containing functional groups of graphene. These spectroscopic observations confirm that the strengthened interfacial adhesion within the NC–Gr–A structure primarily originates from the extensive hydrogen-bonding interactions within the –OH-rich components. Overall, the strong interfacial adhesion and mechanical cohesion of the NC–Gr–A enable the formation of flexible multilayer tribocomponent assemblies that can conform seamlessly to complex surfaces, such as the contours of the human body.

Fig. 2h shows the variations in the generated output voltage of the NC–Gr–A TENG with varying load resistance values ranging from 2 MΩ to 2 GΩ. The corresponding power values measured are shown in Fig. S15. Moreover, Fig. 2i shows the calculated power density for the same load resistance values, reaching a maximum power density of ~5.76 Wm^{-2}, for NDCNC-TENG (at 60 MΩ), a fivefold higher value than TOCNF (1.23 Wm^{-2}). In addition, CNF and SDCNC-based TENG also exhibited lower power output compared to NDCNC, with a peak power density output of 3.17 Wm^{-2} (power output: 2.4 W) and 2.76 Wm^{-2} (power output: 2.8 mW), respectively. Hence, one can consider the positioning of different NCs in the series as NDCNC > CNF > SDCNC > TOCNF in the increasing order of tribopositive nature.

Evaluating the TENG performance under continuous operation is crucial for use in wearable devices. Fig. 2j shows the voltage output of the NDCNC-based TENG at an interval of 5 minutes while continuously operating it for 40 minutes. As the plot demonstrates, the TENG maintained its output voltage, conforming to its long-term durability. Fig. S16 shows the output voltage of the same device operating at various contact-separation frequencies ranging from 0.3 Hz to 2.8 Hz. To our knowledge, our proposed TENG device yields one of the highest performances using conformable cellulose-based TENGs.[40–45]

3.3 NC–CO bio-TENG

Bioderived TENGs were also fabricated to demonstrate the potential of our approach for use in sustainable solutions. Fabrication of bio-TENG requires both frictional triboelectric layers to be bio-derived with a high surface potential difference, leading to high power output, which is rather difficult to achieve since most biopolymers are tribo-positive by nature. In the previous sections, the fabricated TENGs utilized PI as a negative tribolayer, which is a synthetic, non-degradable, and non-recyclable material. To demonstrate the applicability of the proposed triboelectric component on "green" TENG devices, a bioderived tribonegative component was employed.

Recently, we demonstrated the synthesis of highly tribonegative films composed of siloxane-modified castor oil (CO) for fabricating bioderived TENGs.[26] CO, like other biopolymers, is known to have positive triboelectric characteristics. However, modification with silane coupling agents (*i.e.*, 3-(trimethoxysilyl)propyl-methacrylate and vinyltriethoxysilane), can yield an interconnecting siloxane network rendering CO highly tribonegative (Fig. 3a).[26] The reversal from tribopositive to tribonegative behavior originates from the formation of surface-polarized Si–O–Si and Si–O–C linkages introduced by siloxane grafting, as confirmed by X-ray photoelectron spectroscopy (XPS) and Fourier Transform Infrared spectroscopy (FTIR) in our previous study.[26] These bonds possess strong $Si^{\delta+}$–$O^{\delta-}$ dipoles, where oxygen atoms, bearing high electronegativity and non-bonding lone-pair orbitals, act as localized electron-acceptor sites.[46] Consequently, these oxygen-rich surface dipoles enhance the surface electron affinity and stabilize the accumulation of negative charge during contact electrification. KPFM results in our previous study further confirm the appearance of negative surface potential upon siloxane incorporation. This mechanism aligns well with previous reports showing that Si–O-based materials such as PDMS and siloxane elastomers exhibit a strong electron-accepting nature due to surface oxygen dipoles that facilitate charge trapping and electron stabilization.[46] In summary, siloxane modification alters both the chemical and electronic landscape of the castor oil surface by introducing oxygen-dominant dipoles and lone-pair orbitals that increase electron affinity, thereby flipping its native tribopositive behaviour to tribonegative.

Based on the above, we replaced the tribonegative PI layer in the NC–Gr–A based TENG with a CO-based film to prepare NC–CO bio-TENG, as shown in Fig. 3b. In this configuration, the bio-TENG devices displayed a high output voltage (>200 V), with a maximum peak value obtained for the NDNC (~400 V) (Fig. 3c). Fig. 3d shows the variations in output voltage and power density for the NDCNC-based bio-TENG when subjected to different load values ranging from 1 MΩ to 2 GΩ. Subsequently, the power output in relation to varying load resistance was calculated, yielding a peak power density of 0.54 Wm^{-2}, with a power output of 0.49 mW (Fig. S17). This bio-TENG outperforms previously reported bio-TENGs with biopolymeric/bioderived positive and negative triboelectric layers in terms of voltage and power output.[4,26,47–49]

The power-output capability of the bio-TENG was demonstrated by directly lighting a series of connected LEDs without any additional energy-storage components (Fig. S18 and Video S2). When the device was subjected to periodic mechanical tapping, it generated a sufficiently high voltage to illuminate all

 This journal is © The Royal Society of Chemistry 2025

Open Access Article. Published on 16 December 2025. Downloaded on 1/14/2026 9:01:06 PM.
This article is licensed under a Creative Commons Attribution 3.0 Unported Licence.

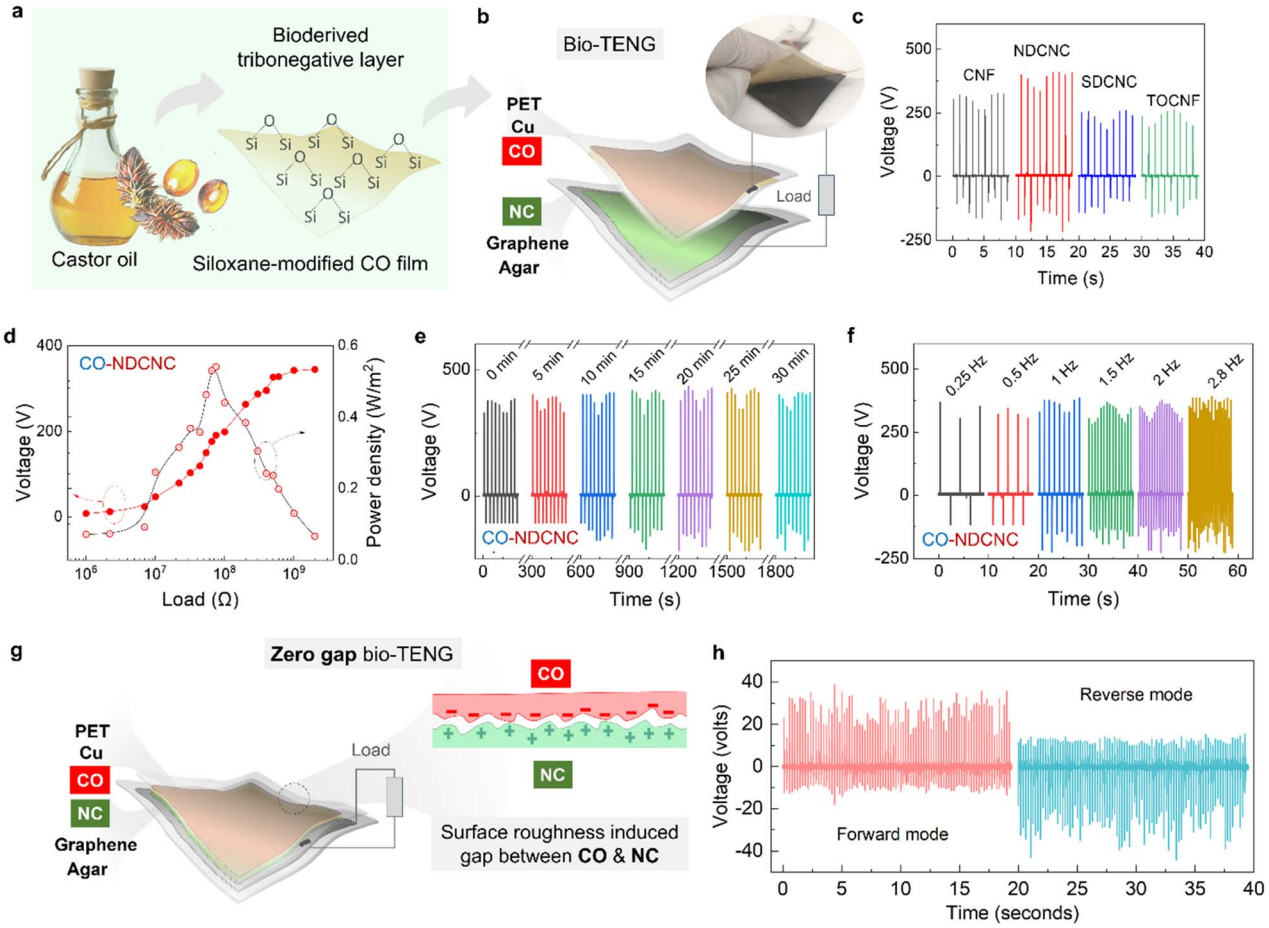

Fig. 3 (a) Schematic of siloxance modified CO film. (b) Schematic representation and photographic image of bio-TENG made of the NC–Gr–A component and CO-based tribonegative layer with both tribocomponents made of bio-derived materials. (c) Device voltage output of the bio-TENG for the different NC (CNF, NDCNC, SDCNC, and TOCNF). (d) Variation of voltage output and power density of the best-performing bio-TENG based on NDCNC and CO as triboelectric layers with varying load resistance values ranging from 1 MΩ to 2 GΩ. (e) Device voltage output of bio-TENG upon continuous operation for 30 minutes. Each dataset was recorded for 10 seconds after every 5 minutes. (f) Plot showing the voltage output response of the bio-TENG at different operating frequencies. (g) Schematic representation of bio-TENG operated in zero-gap mode (ZG-TENG) along with schematic of surface roughness induced nanogap between both bio-derived tribolayers. (h) Voltage output of ZG-TENG in forward and reverse modes.

the LEDs simultaneously, with the on-off light emission remaining steady throughout the test. This demonstration verifies that the bio-TENG can deliver real-time power levels adequate for low-power electronics. In addition, the functional stability of the TENG was assessed by performing a continuous long-term operation (30 min) of the device. The NDNC-based bio-TENG was found to sustain its performance by maintaining its maximum output voltage (Fig. 3e). Moreover, the same device demonstrated output voltage stability across a wide range of operating frequencies, from 0.25 Hz to 2.8 Hz, as shown in Fig. 3f.

The bio-TENG device was also tested in a "Zero-Gap" (ZG) configuration as shown in Fig. 3g. This mode offers an advantage over conventional TENGs, where the gap between the two triboelectric layers is typically in the range of few centimetres. By almost eliminating this distance, a ZG-TENG ensures direct and continuous contact, resulting in a sensitive response to minor deformations or vibrations. Furthermore, unlike typical TENGs, which may have inconsistent contact on curved surfaces, ZG-TENGs can maintain conformability while minimizing unnecessary impact. Even when the triboelectric layers are in direct contact with each other, the roughness-induced gap enables contact and separation between the layers. Therefore, to maintain equilibrium in the system, charge will flow in the external circuit, resulting in an output signal. As shown in Fig. 3h, the maximum voltage output reached a value of 35 V and remained consistent with the electrode polarity switch (forward/reverse mode). In addition, the ZG-TENG was tested under press-release action at varying frequencies, ranging from 1.3 Hz to 5 Hz, while maintaining its TENG performance, as shown in Fig. S19.

The stability of the ZG-TENG was examined in a range of relative humidity (RH) conditions, including 44%, 69%, and 87% (Fig. S20). The output voltage of the ZG-TENG exhibited a noticeable decrease as the humidity levels increased, reaching 35 V at 44% RH, 26 V at 69% RH, and a further sharp drop to

Open Access Article. Published on 16 December 2025. Downloaded on 1/14/2026 9:01:06 PM.
This article is licensed under a Creative Commons Attribution 3.0 Unported Licence.

3.5 V at 87% RH. This decrease in performance at higher RH levels is most likely due to the hygroscopic nature of the agar substrate and the NC layer. Indeed, humidity may affect the interface interactions between the NC–Gr and Gr–A, compromising layer adhesion, as well as charge retention, distribution, and transfer. Although the environmental stability of cellulosic TENGs is a concerning issue in the literature, it can be substantially improved by encapsulating the devices with ultrathin, breathable barrier films that block moisture while preserving flexibility.[50] Incorporating functionalization or interlayers can also enhance their stability, extending operational lifetimes in humid environments.[50,51]

3.4 NC–Gr–A as all-polysaccharide single-electrode TENG (All-PS SE-TENG)

Flexible, all-polysaccharide-based TENGs were developed to operate in a single-electrode configuration (SE-TENG), with NC–Gr–A serving as the active triboelectric component. This component functions effectively against an electrically contact-free triboelectric layer, allowing easier integration with wearable components.

3.4.1 SE-TENG as a touch sensor. The device structure schematic of the single-electrode (SE)-TENG and its integration into a finger touch sensor are shown in Fig. 4a. For these experiments, we utilized NDCNC-based TENG (NC–Gr–A) to achieve better performance and enhanced touch sensing capabilities. The step-by-step operation process and corresponding voltage peak generation mechanism are schematically represented in Fig. 4b. When the NC layer of the NC–Gr–A is brought into contact with another free triboelectric layer, positive and negative static charges are generated on the surface of the NC and the other layer. Upon separation, electrons will flow from the ground towards the graphene electrode, causing an electrical signal. In the case of complete separation, when the charge transfer is done, the external circuit receives no current due to electrical balance. Upon contact, the electrons flow in the reverse direction from the graphene electrode to the ground, resulting in an electrical output in the opposite direction. The fabricated finger-touch sensor was tested against various materials with both tribopositive and tribonegative characteristics relative to the position of NC in the triboelectric series. These materials vary in their ability to donate or accept electrons, producing a distinct voltage response and polarity based on their electron affinity. Fig. 4c shows the comparative output voltage of the touch sensor when NC contacted relatively positive, neutral, and negative materials, such as hair, skin, aluminium, paper, polystyrene (PS), polyethylene (PE), PI, polyvinylidene fluoride (PVDF), and silicone. A variable output voltage amplitude with specific polarity is generated, depending

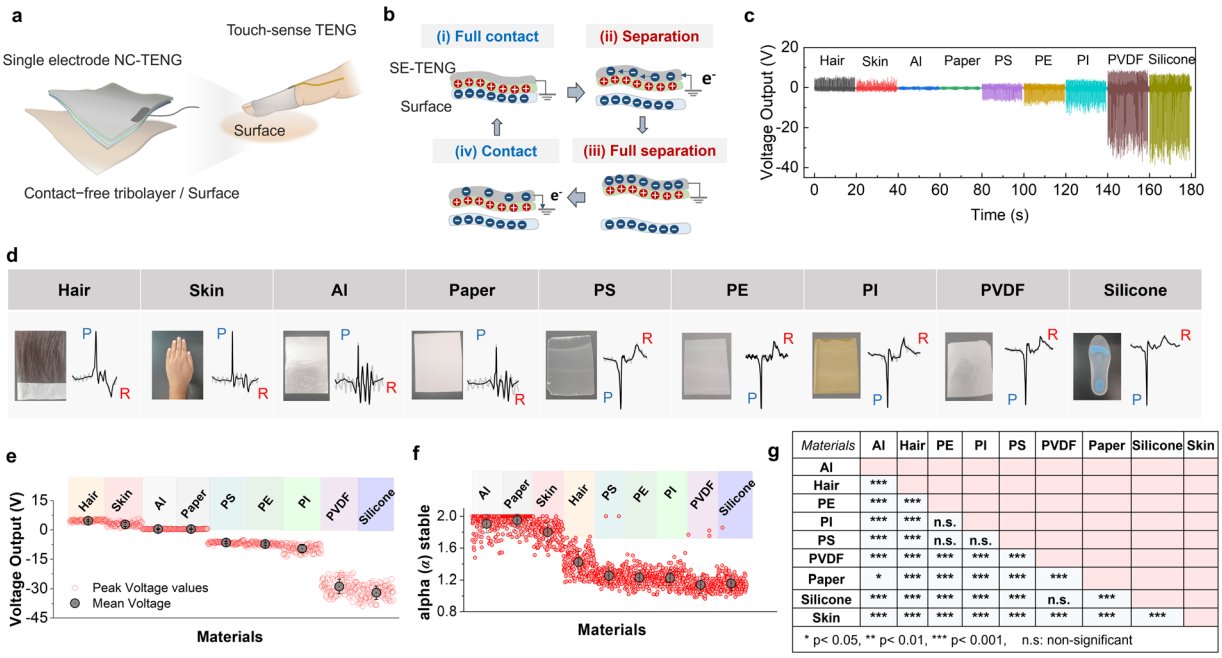

Fig. 4 (a) Schematic representation of NC–Gr–A triboelectric component-based all-polysaccharide-based (single electrode) TENG (All-PS SE-TENG) as a wearable for sensing touch response from materials. (b) Device operation mechanism of the TENG in single electrode mode for testing different materials that are electrically contact-free. (c) The output voltage of NC–Gr–A based All-PS SE-TENG in response to different positive, negative, and highly negative triboelectric materials. Here, hair, skin, aluminum, and paper are positive triboelectric; polystyrene, polyethylene, and PI are slightly negative triboelectric; PVDF and silicone are highly tribonegative in nature. This data is for 100 testing cycles for each material. The comparative plot also highlights the change in the magnitude and polarity of the output voltage upon touching various materials. (d) Single characteristic peak profiles were generated from the SE-TENG device upon physical contact with each material. Figures also show photographs of the corresponding materials. (e) Variation in the magnitude of the peak voltages for 100 cycles for different materials and their average value. (f) Boxplot of the estimated alpha stable (α) parameter for the different materials. (g) Statistical significance table of the estimated α-stable parameter for all pair-wise combinations of the tested materials using the Tukey statistical test.

 This journal is © The Royal Society of Chemistry 2025

Open Access Article. Published on 16 December 2025. Downloaded on 1/14/2026 9:01:06 PM. This article is licensed under a Creative Commons Attribution 3.0 Unported Licence.

on the difference in the electron affinity between NC and the material in contact. Previous works documented that paper, aluminium, skin, and hair are listed as positive triboelectric materials in the series.[52] Thus, paper material appears to be close to the position of NC in the triboelectric series, leading to a minimal difference in the triboelectric potential. Aluminium, besides its positive triboelectric (tendency to lose electrons) behavior, can't retain charges, thus limiting its generated output. As such, both materials exhibited a weak signal, overlapping with stationary noise, which made it challenging to distinguish the voltage output. In contrast, materials such as skin and hair are relatively more tribopositive compared to NC. This difference results in a noticeable positive voltage output when the TENG touch sensor is in contact and during separation. Materials such as PS and PE are typically categorized as positive triboelectric. However, compared to NC, they exhibit a more tribonegative, resulting in relatively low negative voltage outputs. In contrast, materials such as PVDF and silicone exhibited significantly higher performance, with output voltages reaching ~35 V and 40 V, respectively. This superior performance is due to their highly tribonegative nature, positioning them far from NC in the triboelectric series. Based on the systematic evaluation of the polarity and voltage range of the All-PS SE-TENG performance, a triboelectric series was developed based on its interactions with different frictional layers, as illustrated in Fig. S21. Fig. 4d presents photographic images of the test materials and their corresponding single-peak voltage profile when tested against the All-PS SE-TENG. Each material demonstrates a unique voltage output with a specific polarity, reflecting its position in the triboelectric series. Furthermore, Fig. 4e displays the average voltage magnitudes (measured over 100 cycles) and their variations, represented by scattered data points. The materials are arranged from the most tribopositive to the most tribonegative (left to right), highlighting the relationship between the material's triboelectric properties and the output performance of the SE-TENG. This detailed analysis provides insights into optimizing material combinations for enhanced sensing and performance of triboelectric devices.

We have also repeated the measurements multiple times to confirm the reliability of the SE-TENG to sense different testing materials. For each material, we generated four sets of data, totalling 400 testing cycles for each material. Fig. S22 demonstrates the consistency of the SE-TENG when cycled against strongly tribopositive materials (*i.e.*, hair, skin, paper, and Al). During the 400-cycle operation, the device yielded nearly identical peak-to-peak voltages, indicating negligible drift both within and between data sets. A comparable stability in amplitude and polarity is likewise observed when the device operates against materials that are only slightly tribonegative relative to NC (*i.e.*, PS, PE, and PI), confirming the SE-TENG's robust sensing performance across a broad range of contact materials. (Fig. S23). An enhanced voltage peak amplitude was observed for highly tribonegative materials, such as PVDF and silicone, in all sets (Fig. S24), consistent with their hypothesized position in the triboelectric series *versus* NC. Therefore, our All-PS SE-TENG can reliably discriminate among a broad spectrum of contact materials, producing characteristic voltage amplitudes and polarity reversals that reflect each material's position in the triboelectric series.

To further investigate the abovementioned behavior, we performed post-processing analysis in the TENG signal using alpha-stable and symmetric alpha-stable distributions. For that, a univariate distribution function $F(x)$, namely alpha (α)-stable, was expressed in the following form.

$$\varphi(t) = \exp\{jat - \gamma|t|^{\alpha}[1 + j\beta\mathrm{sign}(t)\omega(t,\alpha)]\}, \quad (1)$$

where,

$$\omega(t,\alpha) = \begin{cases} \tan\left(\frac{\alpha\pi}{2}\right) & \text{for } a \neq 1 \\ \frac{2}{\pi}\log|t| & \text{for } \alpha = 1 \end{cases}, \quad (2)$$

and $\mathrm{sign}(t) = 1,0,-1$ for $t > 0$, $t = 0$, $t < 0$), respectively, and

$$-\infty < a < \infty, \gamma > 0, 0 < \alpha \leq 2, -1 \leq \beta \leq 1. \quad (3)$$

These four parameters can completely determine the α-stable distribution: (1) the location parameter a, which is the symmetry axis, (2) the scale parameter γ also called the dispersion, which, in analogy to the variance of the Gaussian distribution, is a measure of the deviation around the mean, (3) the symmetry parameter β, which is the index of skewness, and (4) the characteristic exponent α, which is a measure of the thickness of the tails of the distribution. Thus, a small value of α implies considerable probability mass in the tails of the distribution, while a large value of α implies considerable probability mass in the central location of the distribution. As such, the special cases $\alpha = 2$ and $\alpha = 1$ (with $\beta = 0$) correspond to the Gaussian and Cauchy distributions, respectively. When $\beta = 0$, the distribution is symmetric about the center a, in which case the distribution is called symmetric α-stable, or $S\alpha S$, and its characteristic function takes the following form:

$$\varphi(t) = \exp\{jat - \gamma|t|^{\alpha}\}. \quad (4)$$

For $S\alpha S$ distributions, a is the mean when $1 < \alpha \leq 2$, and the median when $0 < \alpha < 1$.

Fig. 4f presents the estimated a-values for each material, providing a clear visual representation of the impulsive nature of the TENG output signals for the different materials. The estimated a-values serve as a quantifiable metric to capture the impulsiveness inherent in the measured signals, highlighting variations across material groups. Materials like aluminum and paper with a-values close to 2 exhibit Gaussian-like signal behavior characterized by less impulsive outputs. This corresponds to their insufficient retaining and transferring charges, which leads to less pronounced variability in the triboelectric response. As the a-value decreases, the signal becomes more impulsive, with heavier tails in its distribution. This can be observed in the peak profile alteration when the TENG is in contact with bioderived materials such as human skin and hair. The extracted intermediate-range a-values reflect irregularities and variability in the triboelectric interactions, influenced by

Open Access Article. Published on 16 December 2025. Downloaded on 1/14/2026 9:01:06 PM. This article is licensed under a Creative Commons Attribution 3.0 Unported Licence.

the heterogeneous nature of skin and hair, as well as the relatively small difference in electron affinity *versus* NC. Synthetic polymers such as PS, PE, PI, PVDF and silicone exhibit *a*-values around 1.2, indicating highly impulsive signal behavior. These materials, known for their tribonegative character, can generate significant charge differences during contact-separation interactions with NC–Gr–A. Their physical characteristics, such as surface roughness, hydrophobicity, or polarizability, may also contribute to abrupt and pronounced charge generation events. This distinction highlights the sensitivity of the *a*-values in reflecting material-specific characteristics that impact TENG performance.

Furthermore, Fig. 4g compares these material groups through statistical analysis, where the calculated *p*-values indicate statistically significant differences in most cases. These findings confirmed the effectiveness of using *a*-values to differentiate between material groups. Such differentiation can be crucial in identifying the optimal materials for TENG applications, particularly when the quality and consistency of the output signal are paramount. Incorporating the $S\alpha S$ model for signal characterization is an important methodology. Unlike conventional time-domain metrics, such as the number of zero crossings or features based on peak intervals in time series, the $S\alpha S$ model offers a robust approach that is less susceptible to noise interference. Time-domain metrics are often sensitive to environmental noise and signal distortions, resulting in unreliable characterization. In contrast, the $S\alpha S$ model captured the underlying impulsive nature of the signals, providing an alternative and accurate framework for analyzing TENG output. The results justify using $S\alpha S$ as a preferred analytical tool in this context, advancing the signal analysis of TENGs by moving beyond traditional, noise-prone time-based methodologies. Although the estimation of the parameters of α-stable distribution is generally severely hampered by the lack of known closed-form density functions (for all but a few members of the stable family), some numerical methods have been suggested in the literature that perform reliable parameter estimation. For example, the fractile method[53] (adopted here), the regression method,[54] the log $|S\alpha S|$ method, and the negative-order moment method.[55] Future studies involve implementing various *SaS* methods in conjunction with machine learning analysis for accurate event prediction. Overall, the All-PS SE-TENG sensor was found to efficiently distinguish material variations based on two key factors: the magnitude of the output voltage and the polarity of the signal. The same device can generate a range of output voltages without any electrical contribution from the other material. This material behavior identification capability can be particularly valuable for tactile sensing applications, where recognizing various materials through direct contact is advantageous.

3.4.2 SE-TENG as a biomechanical sensor and harvester. The NC–Gr–A tribocomponent can be readily applied to human skin and medical adhesives in a single electrode configuration, facilitating biomechanical sensing and harvesting. The schematic representation of the SE-TENG configuration is shown in Fig. 5a, where friction between the NC film and the silicone insole generates electricity during biomechanical motion, such as walking. This SE-TENG is attached to the sole or plantar region of the foot, the area that contacts the ground to efficiently sense walking motion. Actual images of the device interfaced with the skin are shown, providing both front and side views.

In this configuration, the agar substrate directly interacts with the skin, ensuring comfort. At the same time, the NC layer is exposed to contact with the silicone, facilitating effective triboelectric interaction. This configuration, where the graphene electrode is positioned as an intermediate layer between the dielectric layers of agar and NC, effectively insulates the electrode, preventing direct contact with the body. This safeguards the device against potential short-circuiting or leakage currents while ensuring efficient collection of voltage signals generated during walking. The insulation also minimizes electrical interference and protects the ultrathin graphene electrode from mechanical wear, enhancing signal fidelity and extending the device's lifespan. The conformability of the device also allows it to adapt seamlessly to the contours of the foot's sole, ensuring close contact and optimal performance, even on uneven or curved surfaces.

Fig. 5b presents the laboratory set-up for assessing the reliability and performance of the device in harvesting electrical energy by walking motion under real-world conditions. The testing was conducted with a 52 kg user walking at a frequency of ~1.5 Hz. The device continuously operated over 60 cycles, displaying remarkable consistency and stability in biomechanical energy harvesting (Video S3). Fig. 5c shows the stable output voltage across multiple cycles of walking movement, achieving a peak voltage of ~4 V in response to biomechanical motion. The device was also integrated into the arm using commercially available polyurethane-based medical plasters and tested as a biomechanical energy harvester (see Fig. 5d). To showcase the real-world applicability of the proposed device, we harnessed biomechanical motion through repetitive hand tapping (using a silicone glove) on a TENG-integrated surface to power up multiple (32) LEDs on a flexible breadboard, as shown in Fig. 5e and f (see also Video S4).

In addition to energy applications, it is equally important to ensure effective sweat and moisture absorption while maintaining the capability to allow air and water vapor transmission through the wearables. The water vapor transmission rate (WVTR) of the NC–Gr–A was compared with that of pure agar and FNC film to evaluate its moisture permeability capability. Fig. 5g shows the WVTR of individual triboelectric components along with NC–Gr–A fixed on top of the glass vials (Fig. S25). The WVTR for all films lies in the range of 1500–2250 g/m^2/day. The WVTR of free-standing NDCNC (6 μm) is 2223 g/m^2/day, which is slightly lower than that of the positive control (2350 g/m^2/day), whereas the WVTR of agar (1850 g/m^2/day) and NC–Gr–A (1497 g/m^2/day) is relatively low. The decrease in WVTR for agar and NC–Gr–A is attributed to their thickness, as agar and NC–Gr–A have thicknesses of 100 and 110 μm, respectively, resulting in reduced water vapor permeation compared to the NC film (6 μm thick). The WVTR of NC–Gr–A is comparable to other cellulose-based systems (printing paper and lab coat with a permeability of 1520 g/m^2/day and 1450 g/m^2/day,

 This journal is © The Royal Society of Chemistry 2025

Open Access Article. Published on 16 December 2025. Downloaded on 1/14/2026 9:01:06 PM.
This article is licensed under a Creative Commons Attribution 3.0 Unported Licence.

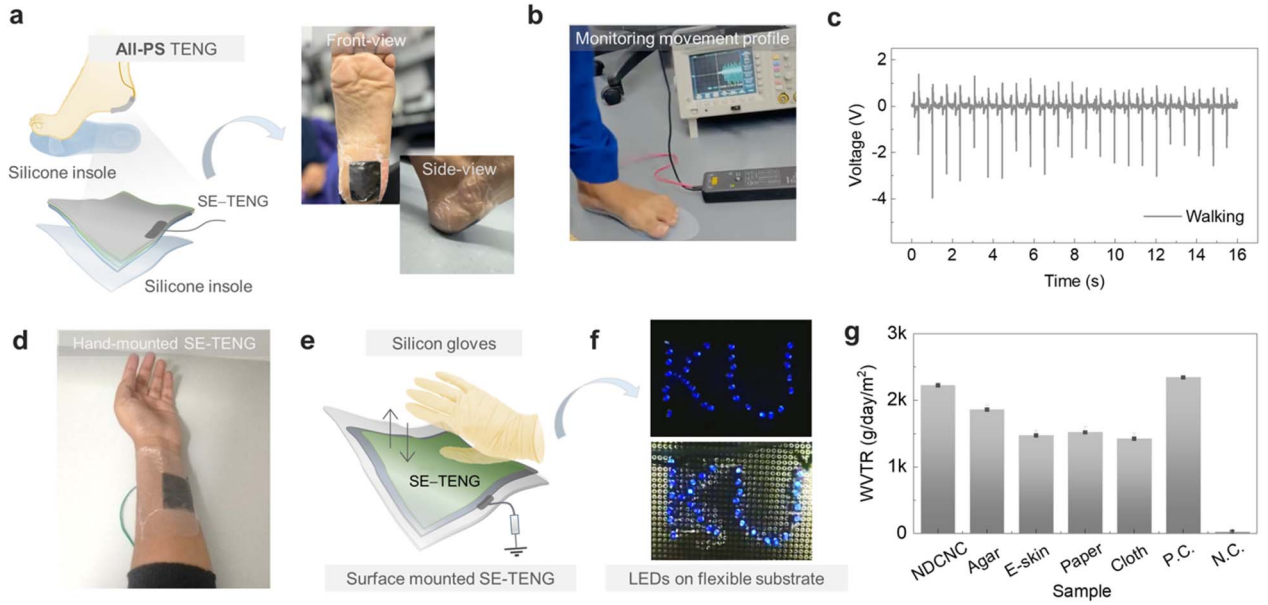

Fig. 5 SE-TENG is a wearable for sensing biomechanical motion in the form of walking. (a) Schematic representation and photograph of SE-TENG integration to the sole of the user's foot, the inferior or bottom surface of the foot, which contacts the floor when standing barefoot. The silicone insole is the other frictional layer with tribonegative characteristics and is electrically contact-free. Photographic image showing the front and side view of the integrated device conforming very well to the contour of the planter region. (b) Laboratory set-up for the study of the reliability of SE-TENG for sensing the kinetic energy of walking in the form of electrical energy. (c) Repeated measurement from SE-TENG in voltage output to evaluate its biomechanical sensing capability and stability: 60 cycles of 52 kg user weight at 1.5 Hz frequency (Video S3). (d) Photo showing the conformability of All-PS SE-TENG when used as a wearable SE-TENG on the hand. (e) Schematic representation of a single electrode configuration of TENG as a power source to light up LEDs using hand tapping while wearing silicone gloves. (f) Powering multiple LEDs connected in series using SE-TENG as energy generators. (g) Water vapor transmission rate (breathability/moisture permeability) of NC–Gr–A triboelectric component along with individual triboelectric components (agar and NC) for wearable and conformable electronics applications, including energy harvesting and sensing.

respectively. Overall, these results show that the WVTR of the NC–Gr–A component and individual components are higher than that of other reported breathable triboelectric layers, as well as human skin (204 g/m^2/day).[56–59] Previously reported air-permeable hydrophobic tribolayers, with low water absorption, fall short of addressing the critical need for moisture management, particularly in hot and humid conditions where sweat is in a liquid state.[60–62] As such, incorporating water-absorbing/hydrophilic layers of NC and agar can significantly enhance the functionality and comfort of TENGs in such environments.[56]

The degradation behaviour of the NC–Gr–A layer was investigated to evaluate its environmental sustainability and transient characteristics. A 1 × 1 cm^2 sample of the film was immersed in a naturally extracted weak acidic solution maintained at 65–70 °C under bath sonication conditions to accelerate the degradation process.

As illustrated in Fig. S26a, the intact film was initially placed in the acidic medium. After 30 minutes of exposure (Fig. S26b), the onset of delamination was observed, indicating the weakening of interfacial adhesion between the NC, Gr, and agar layers. Fragments corresponding to the NC layer (highlighted in black) and agar layer (red) became visible, with graphene adhering to their surfaces. Prolonged exposure for 60 minutes (Fig. S26c) led to further disintegration of the layered structure, resulting in smaller fragments dispersed within the medium. Ultimately, after 120 minutes, complete dissolution of the film occurred (Fig. S26d), leaving no visible solid residues. This systematic degradation highlights the transient and eco-friendly nature of the NC–Gr–A layer, confirming its potential for sustainable disposal under environmentally favourable conditions. Such degradation behaviour supports the concept of green and biodegradable electronics, where the materials can be safely disintegrated without generating persistent waste.

Therefore, the ultrathin component NC–Gr–A based All-PS SE-TENG may be used as a breathable wearable for sensing and energy generation applications without causing inflammation and infection at the wearable site. Therefore, the SE-TENG confirms its potential as a sustainable, environmentally friendly power generation system.

4 Conclusions

In conclusion, this study presented a high-performance triboelectric component developed through an all-solution-processed method, incorporating ultrathin layers of NC (in various forms) as the triboelectric layer and graphene as the electrode, both integrated into a flexible, bio-derived agar substrate. This approach significantly enhanced the performance of cellulosic devices, surpassing traditional fabrication techniques. The thin-layered architecture effectively shortened charge transfer paths and improved interfacial contact, while

Open Access Article. Published on 16 December 2025. Downloaded on 1/14/2026 9:01:06 PM. This article is licensed under a Creative Commons Attribution 3.0 Unported Licence.

the graphene electrodes contributed exceptional conductivity and mechanical flexibility. As summarized in Table S1, these features led to significantly improved device performance compared to previous reports. Additionally, the proposed tribolayers exhibited versatility, adapting to various TENG configurations. In terms of application, the TENGs integrated seamlessly with human skin, enabling real-time biomechanical energy harvesting and touch sensing. Overall, the design approach excelled in performance, processing, and integration, providing a comprehensive pathway for the development of advanced wearable electronics, including biomechanical energy harvesters and self-powered tactile sensors.

Author contributions

BF: writing-original draft, conceptualization, methodology, validation, investigation, data curation. IZ: writing-review & editing, RK: writing-review & editing, RE: writing: review & editing, AG: writing-review & editing, resources. YAS: writing-review & editing, resources, LH: data analysis, writing-review & editing, BLT: writing-review & editing, resources CP: supervision, funding acquisition, resources, writing-review & editing.

Conflicts of interest

There are no conflicts to declare.

Data availability

The data supporting this article have been included in the manuscript and supplementary information (SI). Supplementary information is available. See DOI: **https://doi.org/10.1039/d5ta05646b**.

Acknowledgements

This work was co-funded by Khalifa University, Abu Dhabi, United Arab Emirates, SANDOOQ AL WATAN LLC (SWARD-F23-021), and the National Multiple Sclerosis Society (Project SENSE-MS, NMSS, UAE). This work was also supported by the Advanced Research and Innovation Center (ARIC), which is jointly funded by Aerospace Holding Company LLC, a wholly owned subsidiary of Mubadala Investment Company PJSC, and Khalifa University of Science and Technology. CP also acknowledges the Healthcare Engineering Innovation Center (HEIG).

References

1 D. Liu, J. Luo, L. Huang, M. Chen, M. Ji, Z. L. Wang and J. Kang, *Nano Energy*, 2025, **136**, 110767.
2 T. M. Dip, M. R. A. Arin, H. R. Anik, M. M. Uddin, S. I. Tushar, A. Sayam and S. Sharma, *Adv. Mater. Technol.*, 2023, **8**, 2300802.
3 H. Zhang, L. Xie, Y. Liu, Z. Chen, Z. Gao, Y. Peng, C. Qiao, S. Gao, Z. Fu, P. Jiang, R. Yang, X. Sun and Z. Wen, *Nano Energy*, 2025, **137**, 110810.
4 B. Fatma, S. M. Andrabi, S. Gupta, V. Verma, A. Kumar, C. Pitsalidis and A. Garg, *Nano Energy*, 2023, **114**, 108628.
5 N. Madathil, A. Babu, M. Velupula, A. Kulandaivel, R. K. Rajaboina, U. K. Khanapuram, K. C. Devarayapalli and D. S. Lee, *Sustainable Energy Fuels*, 2025, **9**, 4364–4374.
6 Y. Quan, X. Wu, S. Zhu, X. Zeng, Z. Zeng and Q. Zheng, *Med. Nov. Technol. Devices*, 2022, **16**, 100195.
7 A. Babu, N. Madathil, R. K. Rajaboina, H. Borkar, K. C. Devarayapalli, Y. K. Mishra, S. Hajra, H. J. Kim, U. K. Khanapuram and D. S. Lee, *Mater. Adv.*, 2025, **6**, 4725–4737.
8 Y. Zou, V. Raveendran and J. Chen, *Nano Energy*, 2020, **77**, 105303.
9 L. Xia, H. Zhou, J. Chen, F. Liu, S. Chang, Y. Huang, J. Jiang, K. Dong, Y. Wu, C. Zhang, W. Xuan, S. Dong and J. Luo, *Adv. Electron. Mater.*, 2024, **10**, 2300713.
10 X. Qin, H. Shi, Z. Wen, B. Chu, H. Li, H. Wang, Y. He and X. Sun, *Adv. Healthcare Mater.*, 2024, **13**, 2303474.
11 J. Lu, L. Xu, D. Hazarika, C. Zhang, J. Li, J. Wu, K. Zhang, R. Wan, X. Xu, J. Chen, H. Jin, S. Dong, Y. Huang, Q. Zhang, Y. Wu and J. Luo, *Nano Energy*, 2024, **129**, 110022.
12 F. Fatima, B. Fatma and M. J. Akhtar, *IEEE Asia-Pacific Microwave Conference (APMC)*, 2024, pp. 1314–1316.
13 R. K. Rajaboina, U. K. Khanapuram and A. Kulandaivel, *Adv. Sens. Res.*, 2024, **3**, 2400045.
14 D. Tao, P. Su, A. Chen, D. Gu, M. Eginligil and W. Huang, *npj Flexible Electron.*, 2025, **9**, 4.
15 S. Chang, F. Liu, J. Chen, L. Xia, H. Zhou, J. Jiang, K. Dong, C. Zhang, Y. Wu, J. Chen, W. Xuan, L. Sun, H. Jin, S. Dong and J. Luo, *Sci. China: Technol. Sci.*, 2024, **67**, 949–957.
16 S. Liu, W. Tong, C. Gao, Y. Liu, X. Li and Y. Zhang, *J. Mater. Chem. A*, 2023, **11**, 9270–9299.
17 K. Y. Song, S.-W. Kim, D. C. Nguyen, J. Y. Park, T. T. Luu, D. Choi, J. M. Baik and S. An, *EcoMat*, 2023, **5**, e12357.
18 V. Slabov, S. Kopyl, M. P. Soares dos Santos and A. L. Kholkin, *Nano-Micro Lett.*, 2020, **12**, 42.
19 S. Gupta, C. Chatterjee, B. Fatma, K. Brajesh, R. Bhunia, N. S. Sowmya, S. Roy, A. Kulkarni, R. K. Gupta, R. Gupta, P. M. Ajayan and A. Garg, *ACS Appl. Mater. Interfaces*, 2023, **15**, 26563–26575.
20 S.-J. Park, M.-L. Seol, S.-B. Jeon, D. Kim, D. Lee and Y.-K. Choi, *Sci. Rep.*, 2015, **5**, 13866.
21 R. Yang, *Heliyon*, 2024, **10**, e32361.
22 B. Fatma, R. Bhunia, S. Gupta, A. Verma, V. Verma and A. Garg, *ACS Sustain. Chem. Eng.*, 2019, **7**, 14856–14866.
23 S. Shafeek, N. T. M. Balakrishnan, B. Fatma, A. Garg, J. F. M. J, D. Morton, J. Luo and P. Raghavan, *Nano Energy*, 2023, **107**, 108146.
24 S. Nuthalapati, A. Chakraborthy, I. Arief, K. K. Meena, K. R. Kaja, R. R. Kumar, K. U. Kumar, A. Das, M. E. Altinsoy and A. Nag, *IEEE J. Flex. Electron.*, 2024, **3**, 393–400.
25 R. Zhang, C. Dahlström, H. Zou, J. Jonzon, M. Hummelgård, J. Örtegren, N. Blomquist, Y. Yang, H. Andersson, M. Olsen, M. Norgren, H. Olin and Z. L. Wang, *Adv. Mater.*, 2020, **32**, 2002824.

 This journal is © The Royal Society of Chemistry 2025

Open Access Article. Published on 16 December 2025. Downloaded on 1/14/2026 9:01:06 PM. This article is licensed under a Creative Commons Attribution 3.0 Unported Licence.

26 K. K. Jena, B. Fatma, S. S. Arya, S. M. Alhassan, V. Chan, A. M. Pappa and C. Pitsalidis, *J. Mater. Chem. A*, 2024, **12**, 8340–8349.
27 E. Martín-López, M. Darder, E. Ruiz-Hitzky and M. Nieto Sampedro, *Bio-Med. Mater. Eng.*, 2013, **23**, 405–421.
28 S. Roy and J.-W. Rhim, *Food Hydrocolloids*, 2019, **94**, 391–398.
29 J. Gong, J. Li, J. Xu, Z. Xiang and L. Mo, *RSC Adv.*, 2017, **7**, 33486–33493.
30 B. Zhao, L. Jiang, X. Zeng, K. Zhang, M. M. F. Yuen, J.-B. Xu, X.-Z. Fu, R. Sun and C.-P. Wong, *J. Mater. Chem. A*, 2016, **4**, 14595–14604.
31 R. B. Valapa, G. Pugazhenthi and V. Katiyar, *RSC Adv.*, 2015, **5**, 28410–28423.
32 A. Goswami, K. M. Alam, P. Kumar, P. Kar, T. Thundat and K. Shankar, *Carbohydr. Polym.*, 2020, **246**, 116393.
33 Y. Liu, Q. Fu, J. Mo, Y. Lu, C. Cai, B. Luo and S. Nie, *Nano Energy*, 2021, **89**, 106369.
34 N. Wang, D. Yang, W. Zhang, M. Feng, Z. Li, E. Ye, X. J. Loh and D. Wang, *ACS Appl. Mater. Interfaces*, 2023, **15**, 997–1009.
35 K. W. Klockars, L. G. Greca, J. Majoinen, K. Mihhels, O. J. Rojas and B. L. Tardy, *Carbohydr. Polym.*, 2023, **303**, 120465.
36 A. Babu, S. Gupta, R. Katru, N. Madathil, A. Kulandaivel, P. Kodali, H. Divi, H. Borkar, U. K. Khanapuram and R. K. Rajaboina, *Energy Technol.*, 2024, **12**, 2400796.
37 Z. Wang, W. Liu, J. Hu, W. He, H. Yang, C. Ling, Y. Xi, X. Wang, A. Liu and C. Hu, *Nano Energy*, 2020, **69**, 104452.
38 O. Faruk, M. R. Islam, S. M. S. Rana, G. B. Pradhan, H. Kim, M. Asaduzzaman, T. Bhatta and J. Y. Park, *Nano Energy*, 2024, **127**, 109787.
39 R. D. I. G. Dharmasena, *Nano Energy*, 2020, **76**, 105045.
40 H. G. Menge, N. D. Huynh, H. J. Hwang, S. Han, D. Choi and Y. T. Park, *ACS Energy Lett.*, 2021, **6**, 2451–2459.
41 F. Wang, S. Wang, Y. Liu, S. Ouyang, D. Sun, X. Yang, J. Li, Z. Wu, J. Qian, Z. Zhao, L. Wang, C. Jia and S. Ma, *Nano Lett.*, 2024, **24**, 2861–2869.
42 B. Fatma, S. Gupta, C. Chatterjee, R. Bhunia, V. Verma and A. Garg, *J. Mater. Chem. A*, 2020, **8**, 15023–15033.
43 T. Wang, S. Li, X. Tao, Q. Yan, X. Wang, Y. Chen, F. Huang, H. Li, X. Chen and Z. Bian, *Nano Energy*, 2022, **93**, 106787.
44 H.-J. Kim, E.-C. Yim, J.-H. Kim, S.-J. Kim, J.-Y. Park and I.-K. Oh, *Nano Energy*, 2017, **33**, 130–137.
45 Y. Shao, C.-p. Feng, B.-w. Deng, B. Yin and M.-b. Yang, *Nano Energy*, 2019, **62**, 620–627.
46 M. Voronkov, Y. Yuzhelevskii and V. Mileshkevich, *Russ. Chem. Rev.*, 2007, **44**, 355.
47 W. Jiang, H. Li, Z. Liu, Z. Li, J. Tian, B. Shi, Y. Zou, H. Ouyang, C. Zhao, L. Zhao, R. Sun, H. Zheng, Y. Fan, Z. L. Wang and Z. Li, *Adv. Mater.*, 2018, **30**, 1801895.
48 S. Parandeh, M. Kharaziha and F. Karimzadeh, *Nano Energy*, 2019, **59**, 412–421.
49 Q. Zheng, Y. Zou, Y. Zhang, Z. Liu, B. Shi, X. Wang, Y. Jin, H. Ouyang, Z. Li and Z. L. Wang, *Sci. Adv.*, 2016, **2**, e1501478.
50 J. Zhang, C. Boyer and Y. X. Zhang, *Small*, 2024, **20**, 2401846.
51 N. Wang, Y. Zheng, Y. Feng, F. Zhou and D. Wang, *Nano Energy*, 2020, **77**, 105088.
52 C. H. Park, J. K. Park, H. S. Jeon and B. C. Chun, *J. Electrost.*, 2008, **66**, 578–583.
53 J. H. McCulloch, *Commun. Stat. Simulat. Comput.*, 1986, **15**, 1109–1136.
54 I. A. Koutrouvelis, *Commun. Stat. Simulat. Comput.*, 1981, **10**, 17–28.
55 C. L. Nikias and M. Shao, *Signal Processing with Alpha-Stable Distributions and Applications*, Wiley-Interscience, New York, USA, 1995.
56 R. Rathinamoorthy, T. Aarthi, C. A. Aksaya Shree, P. Haridharani, V. Shruthi and R. L. Vaishnikka, *J. Nat. Fibers*, 2021, **18**, 1857–1870.
57 M. Fernandes, M. Gama, F. Dourado and A. P. Souto, *Microb. Biotechnol.*, 2019, **12**, 650–661.
58 X. Guan, B. Xu, M. Wu, T. Jing, Y. Yang and Y. Gao, *Nano Energy*, 2021, **80**, 105549.
59 R. Rathinamoorthy, *J. Nat. Fibers*, 2021, **18**, 1857–1870.
60 N. Sun, G.-G. Wang, H.-X. Zhao, Y.-W. Cai, J.-Z. Li, G.-Z. Li, X.-N. Zhang, B.-L. Wang, J.-C. Han, Y. Wang and Y. Yang, *Nano Energy*, 2021, **90**, 106639.
61 Y. Li, Z. Zhu, J. Yu and B. Ding, *ACS Appl. Mater. Interfaces*, 2015, **7**, 13538–13546.
62 Y. Zheng, Y. Li, Y. Zhao, X. Lin, S. Luo, Y. Wang, L. Li, C. Teng, X. Wang, G. Xue and D. Zhou, *Nano Energy*, 2023, **107**, 108092.